ADVANCED ENERGY MATERIALS
www.advenergymat.de

Comprehensive Analysis of Anode-Less Batteries with Lithiophilic Seeds in Liquid and Solid-State Electrolytes

Jihoon Oh, Jisub Kim, Sangjin Bae, Heejin Kim, Taeyong Lee, Seung Ho Choi, Gaeun Park, Seohan Ji, Ki Jae Kim, and Jang Wook Choi**

Anode-less batteries, by eliminating the need for conventional active materials on the anode to thereby maximize the energy density and manufacturing efficiency, are at the frontier of next-generation electrochemical energy storage. Attempts to mitigate lithium (Li) dendrite formation, a persistent problem, have prompted extensive investigations into the use of lithiophilic seed layers on the anode current collector. This paper presents a systematic evaluation of diverse lithiophilic metal thin films as protective interlayers by analyzing their electrochemical and structural behaviors in both liquid and solid electrolyte environments. Liquid electrolyte systems universally undergo rapid capacity decay regardless of the chosen metal, whereas solid-state systems demonstrate material-dependent cyclability, with the cycle life predominantly limited by their susceptibility to internal short circuits. This limitation is overcome by developing a dual-solid electrolyte architecture combined with Li interfacial energy control to significantly enhance the critical current density. This approach enables stable room-temperature operation of anode-less all-solid-state batteries with 82.8% capacity retention over 150 cycles. This comprehensive investigation elucidates the critical dual role of metal interlayers and the physical state of the electrolyte in governing the performance of anode-less batteries, and establishes fundamental design principles for advanced anode-less systems.

1. Introduction

Advanced energy storage systems are becoming indispensable in view of the increasing electrification of transport and the demand for renewable energy storage, and have catalyzed intensive research into secondary batteries with superior energy density.[1] Anode-less battery architectures, which have emerged as a disruptive strategy in this pursuit, are designed to circumvent conventional intercalation-[2] or alloy-based[3] anode materials to enhance the energy density while simultaneously lightening manufacturing processes and improving the cost efficiency.[4] These systems maximize the capacity utilization per volume by enabling the direct deposition of lithium (Li) metal on the anode current collector during charging.[5] However, this paradigm introduces a critical limitation: the absence of prestored active materials facilitates uncontrolled Li dendrite formation.[6] These dendritic structures compromise the electrochemical stability, accelerate capacity fading, and pose significant safety concerns due to the heightened risk of internal short-circuiting.[7] Contemporary research primarily focuses on engineering multifunctional protective interfaces on the anode substrate to address these challenges.[8] These specialized layers regulate the Li-ion flux, promote homogeneous nucleation, and suppress dendrite propagation, thereby addressing both the performance degradation and safety limitations inherent to anode-less designs.[9]

A prototypical example of this approach is the incorporation of silver–carbon (Ag–C) composite layers.[10] The lithiophilic Ag component reduces the Li nucleation overpotential during initial charging to facilitate spatially uniform deposition through favorable alloying interactions.[11] Concurrently, the carbon matrix

J. Oh, J. Kim, S. Bae, T. Lee, G. Park, S. Ji, J. W. Choi
School of Chemical and Biological Engineering and Institute of Chemical Process
Seoul National University
Seoul 08826, Republic of Korea
E-mail: jangwookchoi@snu.ac.kr
J. Oh, J. Kim, S. Bae, G. Park, J. W. Choi
Hyundai Motor Group-Seoul National University (HMG-SNU) Joint Battery Research Center (JBRC)
Seoul National University
Seoul 08826, Republic of Korea
H. Kim
Division of Analytical Science
Korea Basic Science Institute
Daejeon 34133, Republic of Korea
S. H. Choi
Advanced Batteries Research Center
Korea Electronics Technology Institute
Seongnam-si 13509, Republic of Korea
K. J. Kim
Department of Energy Science
Sungkyunkwan University
Suwon-si, Gyeonggi-do 16419, Republic of Korea
E-mail: kijaekim@skku.edu
The ORCID identification number(s) for the author(s) of this article can be found under https://doi.org/10.1002/aenm.202502711

DOI: 10.1002/aenm.202502711

serves as a multifunctional barrier that physically restricts dendrite propagation while passivating the Li–electrolyte interface against parasitic side reactions to counteract the high conductivity of the metallic surface of the current collector. When integrated with solid-state electrolytes, this engineered architecture achieved exceptional cycling performance by effectively addressing the persistent challenge of rapid capacity fading in anode-less configurations.

The strategic incorporation of lithiophilic nucleation seeds has emerged as a cornerstone of anode-less battery design, with metallic coatings (e.g., Ag,[12] Mg,[13] Sn[14]) demonstrating particular efficacy. Thin-film configurations (<1000 nm) of lithiophilic metals present a synergistic design that maximizes the energy density while preserving the electrode processability. To elucidate the role of metal selection in the performance of the protective layer, in this study, we systematically evaluated six distinct lithiophilic (Li-miscible) metals as thin-film modifiers and assessed their electrochemical behavior in both liquid and solid-state electrolyte environments. As a result, in liquid electrolytes, all the metallic films exhibited universally poor Coulombic efficiencies (CEs) and experienced rapid capacity loss, regardless of their lithiophilicity. Although the lithiophilic seeds initially facilitate uniform nucleation, the liquid electrolyte is in contact with the deposited Li across the entire surface, while expanding Li clusters continuously expose fresh regions of the metallic surface. This process accelerates parasitic side reactions, including electrolyte decomposition and the formation of electrochemically inactive ("dead") Li. This irreversible consumption mechanism predominates regardless of the type of metal seed used.

In stark contrast, the solid-state electrolytes demonstrated fundamentally distinct failure mechanisms. The cycle life correlated directly with the lithiophilic metal selection and was predominantly governed by failure due to internal short-circuiting. Unlike liquid electrolytes, in solid-state systems, the Li–electrolyte interface is confined to a 2D plane, which significantly limits the extent of the reactive interface. In other words, from the perspective of electrolyte mobility, whereas liquid electrolyte systems continue to destabilize "hot" spots at the interface due to the fluidity of the electrolyte, unstable interfacial spots in solid-state electrolyte systems are less prone to uncontrolled side reactions owing to the immobility of the solid-state electrolyte. Hence, the fluidity of the electrolyte determines the interfacial geometry and thus the controllability of reactivity therein.

To overcome premature failure in all-solid-state batteries (ASSBs), as represented by the occurrence of short circuits, we engineered a dual-layer solid electrolyte architecture[15] coupled with a solid electrolyte additive that modulates the Li interfacial energy. This system achieved a critical current density (CCD) of 2.9 mA cm^{-2}, which represents an improvement of 322% over the baseline solid electrolytes. This approach enables stable room-temperature operation of anode-less ASSBs with 82.8% capacity retention over 150 cycles.

By decoupling the roles of the metal protective layer and the physical state of the electrolyte (liquid or solid), this work establishes two universal design criteria for anode-less batteries: 1) integration of the solid electrolyte with the geometrically confined Li–electrolyte interface to minimize the electrolyte contact area and detrimental parasitic reactions; and 2) development of hierarchical protective interfaces that combine lithiophilic nucleation for guiding Li plating (via metal films), and mechanical rigidity to prevent dendrite penetration (via solid electrolyte layer design). These principles resolve the conflicting requirements for energy density and sustainability in anode-less systems, and present new ideas toward expediting their practical implementation.

2. Results and Discussion

Lithiophilicity refers to the degree of affinity for Li, which relates to the Li nucleation overpotential during charging. High lithiophilicity promotes uniform Li deposition by stabilizing initial nucleation through thermodynamically favorable alloy phase formation.[16] Metals that are highly soluble in Li—as corroborated by their phase diagrams—are typically classified as lithiophilic. To elucidate the efficacy of lithiophilic metals as a protective layer for the anode-less electrode, we systematically investigated six candidates that form binary phases with Li according to their respective phase diagrams: silver (Ag), aluminum (Al), indium (In), magnesium (Mg), tin (Sn), and zinc (Zn). A layer of each of these metals (thickness: 100 nm) was deposited on a copper (Cu) current collector to establish a 2D protective interface, followed by comprehensive electrochemical evaluation and physicochemical analyses. Given the ultrathin seed layer employed, the lithiophilicity of the seed material and its resultant initial Li nucleation behavior critically govern overall cell performance. Characterization via scanning electron microscopy (SEM) (Figures S1 and S2, Supporting Information) and time-of-flight secondary ion mass spectrometry (ToF-SIMS) (Figure S3, Supporting Information) confirmed the uniformity and the designated thickness of the deposited thin-films.

The electrochemical performance was assessed in a liquid electrolyte (3 M Li bis(fluorosulfonyl)imide (LiFSI) in dimethylsulfamoyl fluoride (FSA; fluorosulfonamide)) using a half-cell configuration (**Figure 1**). Li plating/stripping cycles, conducted at 1 mA cm^{-2} with a 1 h duration for each Li plating, revealed lower Li nucleation overpotential ($\eta_{nucleation}$) for Ag, In, Sn, and Zn compared to bare Cu (Figure S4, Supporting Information), while Al and Mg exhibited higher $\eta_{nucleation}$ (Figure 1a,f). This elevation is attributed to interfacial resistance from native oxide layers,[17] resulting from the low standard reduction potentials of Mg and Al (Figure S5, Supporting Information), as confirmed by diminished overpotentials postinitial cycle or under low-current conditions (Figures S6 and S7, Supporting Information). Extended cycling revealed that the CE for most metals stabilized ≈99.0% (Figure 1g), implying the inadequacy of these anode-less electrodes in full-cells: Li solely sourced from the cathode would lead to cumulative losses, which would severely degrade the capacity retention.

To quantify the reversibility of the individual metal thin-film samples, the cumulative CEs were calculated by multiplying the CE values that were recorded throughout the cycling duration (Figure S8, Supporting Information).[18] These results showed that Ag, In, and Mg demonstrated superior reversibility compared to Al, Sn, and Zn. Nevertheless, even the higher performing metals achieved cumulative CEs lower than 40% after 120 cycles, pointing to pronounced irreversible Li consumption.

Full-cell evaluations with $LiNi_{0.8}Co_{0.1}Mn_{0.1}O_2$ (NCM811) cathodes revealed more severe capacity fading across all metal thin-films (Figure 1h), with the capacity retention dropping below 62%

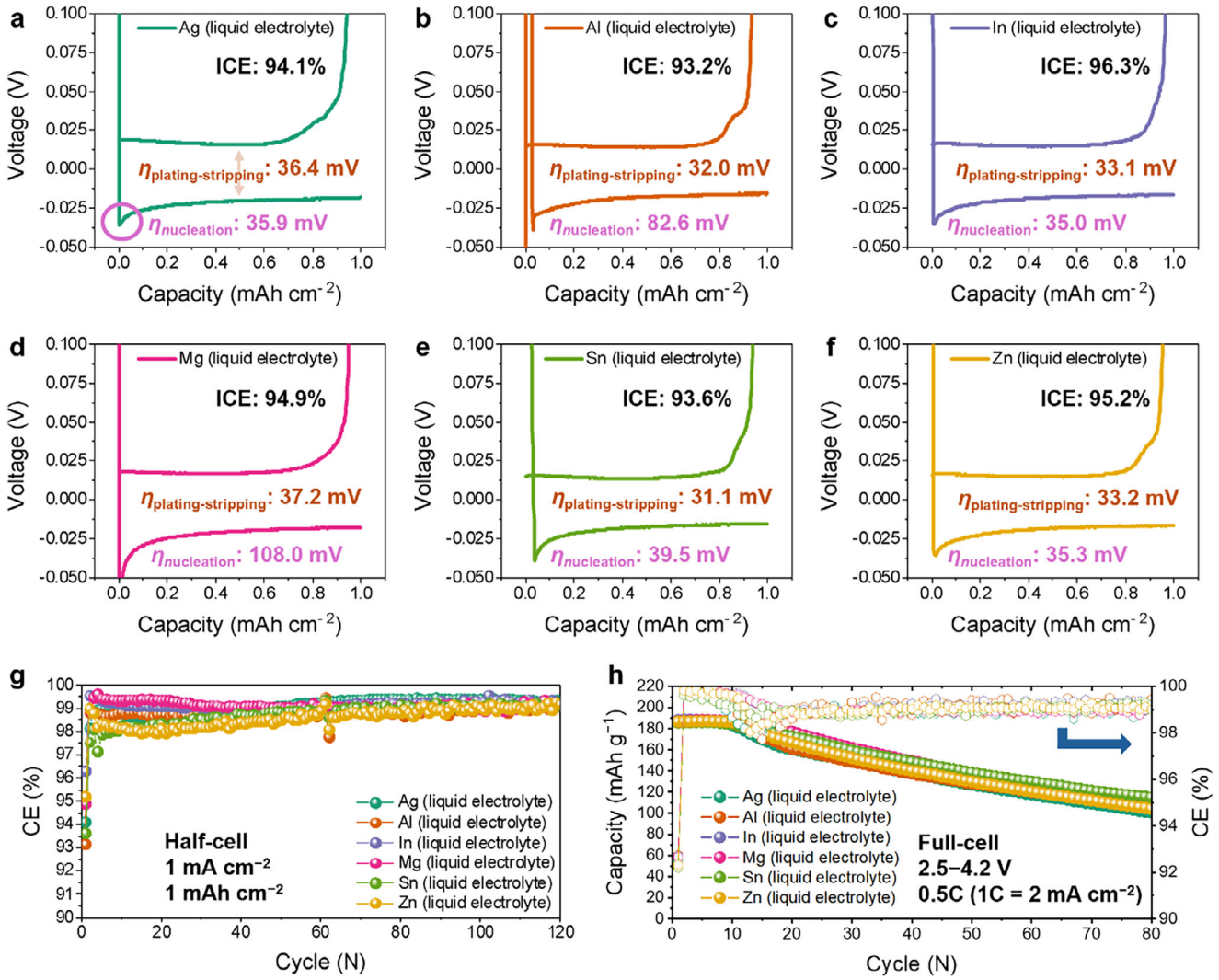

Figure 1. Electrochemical evaluation using a liquid electrolyte (3 M LiFSI in FSA). a–f) First-cycle voltage profiles of half-cells with six different lithiophilic thin-film protection layers (100 nm) on Cu foil. g) Corresponding Coulombic efficiencies (CEs) during Li plating–stripping tests in half-cells at a current density of 1 mA cm^{-2} and a capacity of 1 mAh cm^{-2}. h) Full-cell performance with an NCM811 cathode at 0.5 C (1 C = 2 mA cm^{-2}).

after 80 cycles. Despite the existence of minor performance variations among the metals, the differences were not substantial, suggesting that the cyclability is not predominantly regulated by the choice of metal for the protective layer. Instead, pervasive parasitic reactions—stemming from the extensive 3D Li–electrolyte interfacial contact—are likely a primary factor that determines the reversibility of each cycle.[19]

The influence of the metal selection on the Li deposition behavior was investigated by electrodepositing Li (1 mAh cm^{-2}) at 1 mA cm^{-2} for 1 h onto the different metal layers on the anodeless current collector. Characterization of the morphologies of the resultant top surfaces via SEM (**Figure 2**) showed that the morphology distinctly depended on the underlying metal substrate. The Ag substrate facilitated Li deposits with the finest granularity to yield the largest surface area (Figure 2a). The Al and In substrates produced moderately larger Li grains (Figure 2b,c), whereas the Mg and Sn substrates induced pronounced lateral growth to form substantially coarse Li structures (Figure 2d,e). The Zn substrate promoted the formation of intermediate-sized grains that morphologically resembled those observed on Al and In (Figure 2f). Despite the minimal thickness of the metallic seed layers (100 nm) relative to the deposited Li (≈5 μm), the characteristics of the metallic substrate profoundly influenced the Li growth pattern. Among the investigated metal seeds, Mg exhibited the most uniform Li deposition morphology, and its minimal atomic size mismatch with Li plays a role behind. With an atomic radius of 160 pm compared to Li's 152 pm, the mismatch is only ≈5%, minimizing lattice distortion during alloying. This reduced mismatch results in lower local strain, promoting smooth structural integration between deposited Li and the underlying Mg thin-film host. Nevertheless, electrochemical analyses with liquid electrolytes (Figure 1) revealed consistently low CEs across all the metals, irrespective of their particular deposition morphology. This discrepancy suggests that the interfacial reactivity between Li and liquid electrolytes buries the effect of the deposition morphology, which highlights the inherent

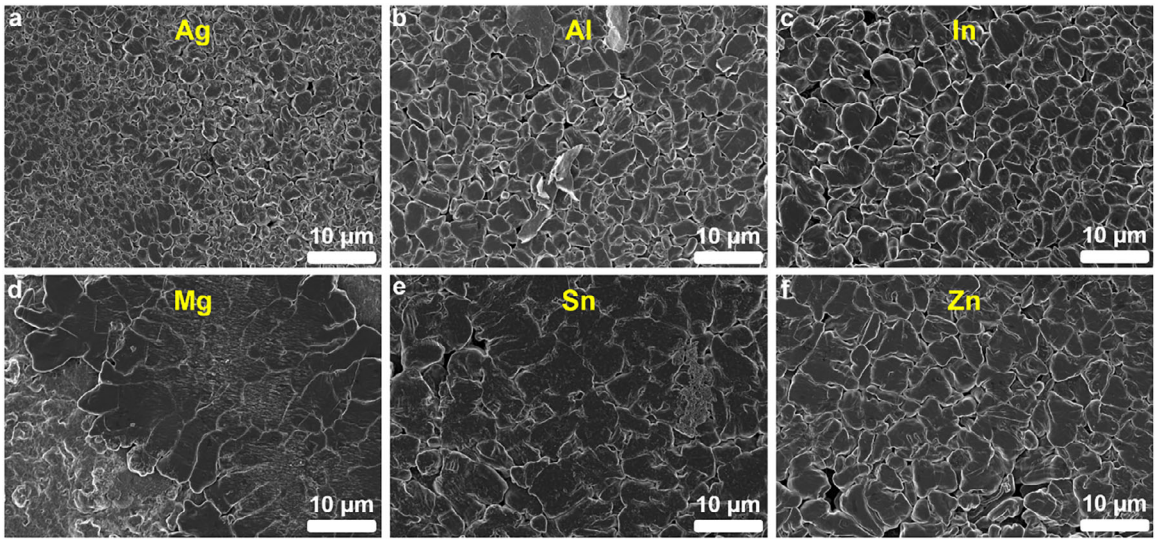

Figure 2. Top-view SEM images after Li deposition at a current density of 1 mA cm^{-2} and a capacity of 1 mAh cm^{-2} for six different lithiophilic thin-film protection layers (100 nm) on Cu foil in a liquid electrolyte system (electrolyte: 3 M LiFSI in FSA).

limitation of employing liquid electrolytes in anode-less battery cells.

We next assessed the six anode-less systems with these metal thin-films in ASSB cells using a sulfide-based argyrodite solid electrolyte (Li_6PS_5Cl, LPSCl). The voltage profiles from the first Li plating–stripping cycles in half-cells (**Figure 3a,f**) revealed a clear difference from their liquid electrolyte-based counterparts. Notably, the difference in the overpotential across the metals was significantly small in the solid electrolyte system. That is, while the liquid electrolytes exhibited pronounced metal-dependent variations in both $\eta_{nucleation}$ and $\eta_{plating-stripping}$ (Figure 1a,f), the solid-state systems demonstrated minimal differences. Furthermore, the overpotential trends changed fundamentally: $\eta_{nucleation}$ decreased in the order of Al > Sn > Mg > In > Zn > Ag, whereas $\eta_{plating-stripping}$ varied in the order of Al = Sn > Ag > In > Zn > Mg—a trend that directly contradicted that in the liquid systems, where Mg consistently exhibited the highest overpotential. This can be attributed to the high pressure (390 MPa) applied during cell assembly, which likely fractures the native oxide layer and thereby promotes direct contact between the Mg surface and the solid electrolyte, effectively reducing the interfacial resistance associated with the oxide layer.[20]

Importantly, half-cell tests at 1 mA cm^{-2} and 1 mAh cm^{-2} revealed metal-dependent cycle life characteristics that were absent in the liquid systems (Figure 3g). Unlike the uniform irreversibility observed with the liquid electrolyte, most metals in the solid-state configuration failed as a result of short-circuiting because of Li infiltration at the grain boundaries of the solid electrolyte that form under nonuniform deposition.[21] Postdeposition SEM analysis confirmed significant seed-dependent variations in Li plating morphology (Figure S9, Supporting Information), with Mg demonstrating the most uniform plating characteristics, followed by Ag. Under applied stack pressure (20 MPa), localized Li protrusions penetrate SE defects, inducing internal short-circuits. This phenomenon accounts for the poor cyclability observed with the seed materials other than Mg and Ag. The common ability of Mg and Ag to form alloys with Li via the solid-solution mechanism rationalizes the superior nature of the solid-solution reaction over the intermetallic reaction in stabilizing anode-less architectures in ASSBs over cycling.[22] Intermetallic compounds consist of discrete phases that suppress Li diffusion across grain boundaries and limit overall Li transport. In contrast, solid-solution alloys establish continuous concentration and chemical potential gradients that enable smooth Li diffusion throughout the material. Particularly notable is that Mg outperformed all the metals by achieving superior CE from the 2nd cycle onward (Figure S10, Supporting Information), and demonstrated an extended cycle life.

The Li plating voltage profiles of ASSB half-cells revealed marked variations across the different metal seeds. During the 1st plating cycle, all seeds displayed an overpotential linked to Li nucleation. Subsequent cycles (2nd and 3rd), however, diverged in behavior depending on the particular seed (Figure S11, Supporting Information). For Ag, Mg, and Sn, the $\eta_{nucleation}$ vanished by the 2nd cycle to be replaced by a gradual rise in the overpotential during continued plating. In contrast, Al, In, and Zn retained $\eta_{nucleation}$ until later cycles. This persisting behavior in the latter three cases suggests that Li is nucleating on lithiophobic substrates[8a] and reflects the inability of these seeds to stabilize Li nucleation and deposition over prolonged cycling.

Even among Ag, Mg, and Sn, distinct trends were observed from the 10th cycle onward (Figure S12, Supporting Information): Ag and Sn began to exhibit $\eta_{nucleation}$, whereas Mg uniquely maintained a smooth voltage profile devoid of nucleation barriers. This trend in the voltage profile of Mg suggests that this metal sustains a lithiophilic interface during prolonged cycling, and that this enables continuous and homogeneous Li nucleation. Such interfacial resilience directly underpins the exceptional reversibility and long-term cyclability of Mg compared to the other seeds.

The disparity in the lifespan between Mg and Ag in ASSB cells is associated with their distinct lithiation behaviors. Mg is prone

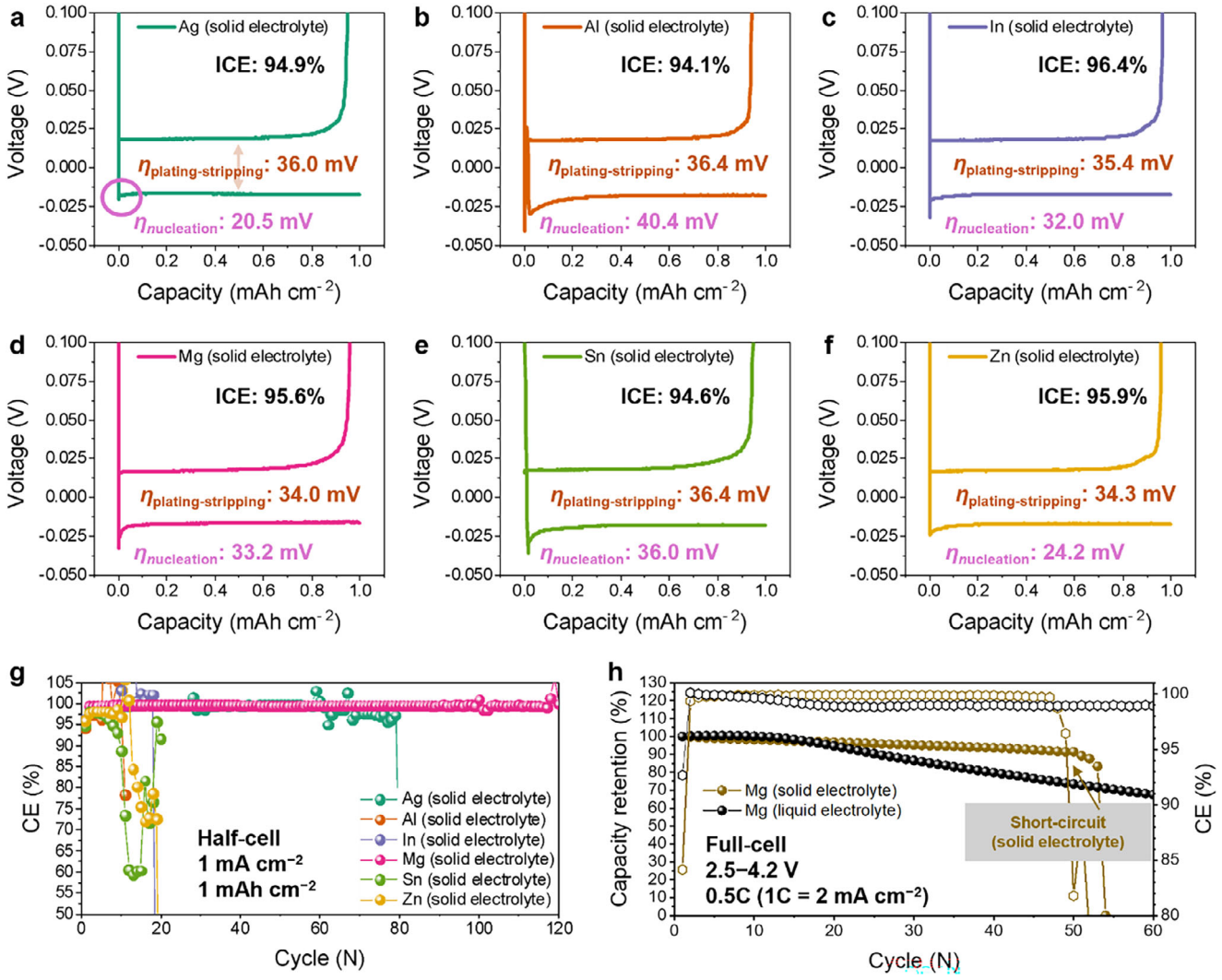

Figure 3. Electrochemical evaluation using a solid electrolyte (Li_6PS_5Cl). a–f) First-cycle voltage profiles of half-cells with six different lithiophilic thin-film protection layers (100 nm) on Cu foil. g) Corresponding Coulombic efficiencies (CEs) during Li plating–stripping tests in half-cells at a current density of 1 mA cm^{-2} and a capacity of 1 mAh cm^{-2}. h) NCM811 full-cell cyclability of the Mg thin-film anode-less protection layer with liquid and solid electrolytes at 0.5 C (1 C = 2 mA cm^{-2}).

to developing a Li concentration gradient (LCG) during lithiation, which generates a thermodynamic driving force that directs Li migration from the surface to the Mg core.[23] The Li–Mg system maintains a single β-phase across a broad Li composition range (>30 at%), enabling continuous, long-range LCGs within the alloy.[24] This phenomenon promotes localized Li accumulation and subsequent Li deposition on the Mg surface. In contrast, Ag undergoes homogeneous lithiation to form a single-phase Ag–Li alloy without LCG formation. This leads to rapid saturation of the alloy phase, followed by the accumulation of unalloyed Li at the top surface. Cross-sectional imaging after Li deposition (5 µm; 1 mAh cm^{-2}) corroborated these mechanisms: Mg remained uniformly dispersed throughout the Li layer (Figure S13, Supporting Information), whereas Ag is localized exclusively at the Li-deposit/substrate interface (Figure S14, Supporting Information). These observations were further supported by ToF-SIMS depth profiling (Figure S15, Supporting Information) and X-ray photoelectron spectroscopy analysis (Figure S16, Supporting Information) at the anode interface. During prolonged cycling, displacement of the Ag seeds from the top surface accelerates the onset of $\eta_{nucleation}$ and promotes inhomogeneous Li growth, thereby heightening the susceptibility to dendrite-induced short circuits.

Given its more reliable reaction behavior with Li, hereafter, we focused our investigation exclusively on Mg. To decouple the effects of stack pressure and Mg seed in ASSB cells, we evaluated cells with and without Mg (bare current collector) at two pressures of 20 and 5 MPa (Figure S17, Supporting Information). Cells lacking seed layer exhibited premature internal short circuits irrespective of applied pressure, directly confirming the indispensable role of Mg as the lithiophilic seed to ensure the cyclability. Conversely, Mg cells demonstrated enhanced reversibility at the elevated stack pressure, establishing that mechanical compression is also critical for anode interfacial stability in anode-less ASSB systems.

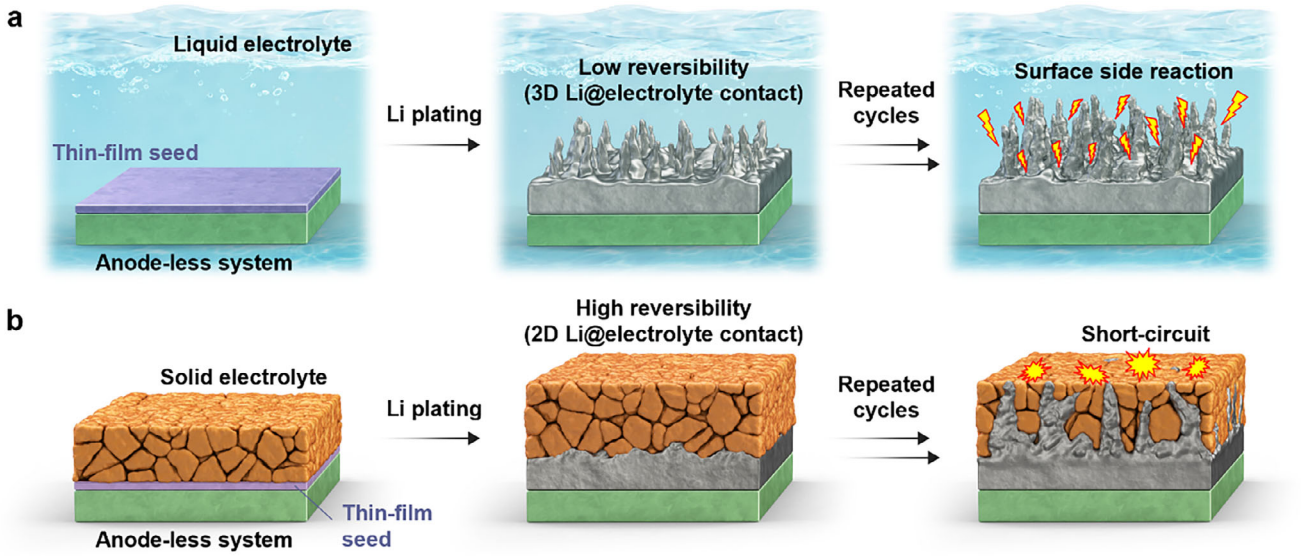

Figure 4. Schematic illustration of Li plating behavior in thin-film seed-based anode-less batteries with a) liquid and b) solid electrolytes.

Cumulative CE measurements in Mg-based half-cells (Figure S18, Supporting Information) demonstrated that the reversibility of the system with the solid electrolyte is significantly higher than that of the liquid electrolyte system. Once again, this difference arose from the distinct geometry at the Li–electrolyte interface: 3D versus 2D. Full-cell evaluations in which Mg thin-films were paired with NCM811 cathodes reconfirmed this trend, as the capacity retention of the corresponding ASSB cells was noticeably enhanced (Figure 3h). However, operation of the solid-state system abruptly ceased because of internal short circuits—a failure mechanism not observed for its liquid electrolyte counterpart—resulting in an operational lifetime shorter than 50 cycles. Cross-sectional SEM imaging coupled with energy dispersive spectroscopy after the 51st Li deposition in the Mg-based ASSB half-cell revealed near-complete overlap between the Mg and S elemental distributions (Figure S19, Supporting Information), the latter originating from the solid electrolyte. This overlap validated extensive Li propagation into the solid electrolyte layer.

In summary, anode-less configurations used in combination with a liquid electrolyte are fundamentally constrained by their low reversibility due to indiscriminate interfacial reactions across their 3D interface, whereas the cycling of solid electrolyte systems is limited by their inherent susceptibility to internal short-circuiting (**Figure 4**). Examination of the morphology after the 51st Li deposition in the Mg-liquid electrolyte system revealed significant structural degradation compared to the initial state (Figure S20, Supporting Information). The Li grains exhibited fibrous morphologies, accompanied by the pronounced accumulation of electrochemically inactive Li deposits. Electrochemical impedance spectroscopy (EIS) and distribution of relaxation times analyses[25] of the Mg-based half-cells further corroborated these observations. In the liquid electrolyte system, the charge transfer resistance (R_{CT}) increased progressively, in reflection of the accumulation of interfacial byproducts over time (Figure S21, Supporting Information).[26] By contrast, in the solid electrolyte system, the decrease in R_{CT} during cycling is likely due to the inevitable penetration of the solid electrolyte layer by Li dendrites, which create internal electronic conduction pathways (Figure S22, Supporting Information).

Given the persistent challenges faced when attempting to improve the reversibility of liquid electrolyte-based anode-less systems, addressing internal short circuits in solid-state configurations would seem to be a more promising direction for anode-less architectures in practice. Along this line, any potential solutions would necessitate optimization of the anode-less protection layer to enhance the CCD value. Toward this end, we devised a dual-layered solid electrolyte structure comprising LPSCl and $Li_{10}SnP_2S_{12}$ (LSPS) (**Figure 5a**) to take advantage of their complementary mechanical properties. In particular, the LSPS interlayer is known to create a "screw effect" driven by the stress gradient,[15] which disrupts dendrite propagation and substantially elevates the CCD. Simultaneously, the integration of lithium fluoride (LiF) into the LPSCl matrix (Figure S23, Supporting Information) increases the Li interfacial energy to effectively repel Li dendrites (dual layer-LiF-LPSCl).[27]

Density functional theory (DFT) calculations to quantify the Li interfacial energy of LPSCl (−33 meV Å^{-2}) and LiF (44 meV Å^{-2}) (Figure 5b) indicated the possibility that the addition of even a minimal amount of LiF would significantly enhance the interfacial repulsion. To validate this approach, symmetric cells were subjected to CCD evaluations by incrementally increasing the current density and fixing the duration per cycle to 1 h (Figure 5c). The pristine LPSCl cell (i.e., without the additive) failed at 0.9 mA cm^{-2} (Figure 5d), yet the dual layer-LiF-LPSCl cell achieved a CCD of 2.9 mA cm^{-2} (Figure 5e). Systematic evaluation of LiF loading revealed that 5 wt% yielded maximum CCD performance (Figure S24, Supporting Information). This represents an improvement of 322% and is attributed to the synergistic suppression of dendrites via both mechanical (the screw effect) and chemical (Li interfacial energy) mechanisms. While dual-layer configurations require additional processing steps that may be unsuitable for large-area fabrication, high interfacial energy additives offer scalability through simple powder mixing compatible with existing manufacturing infrastructure.

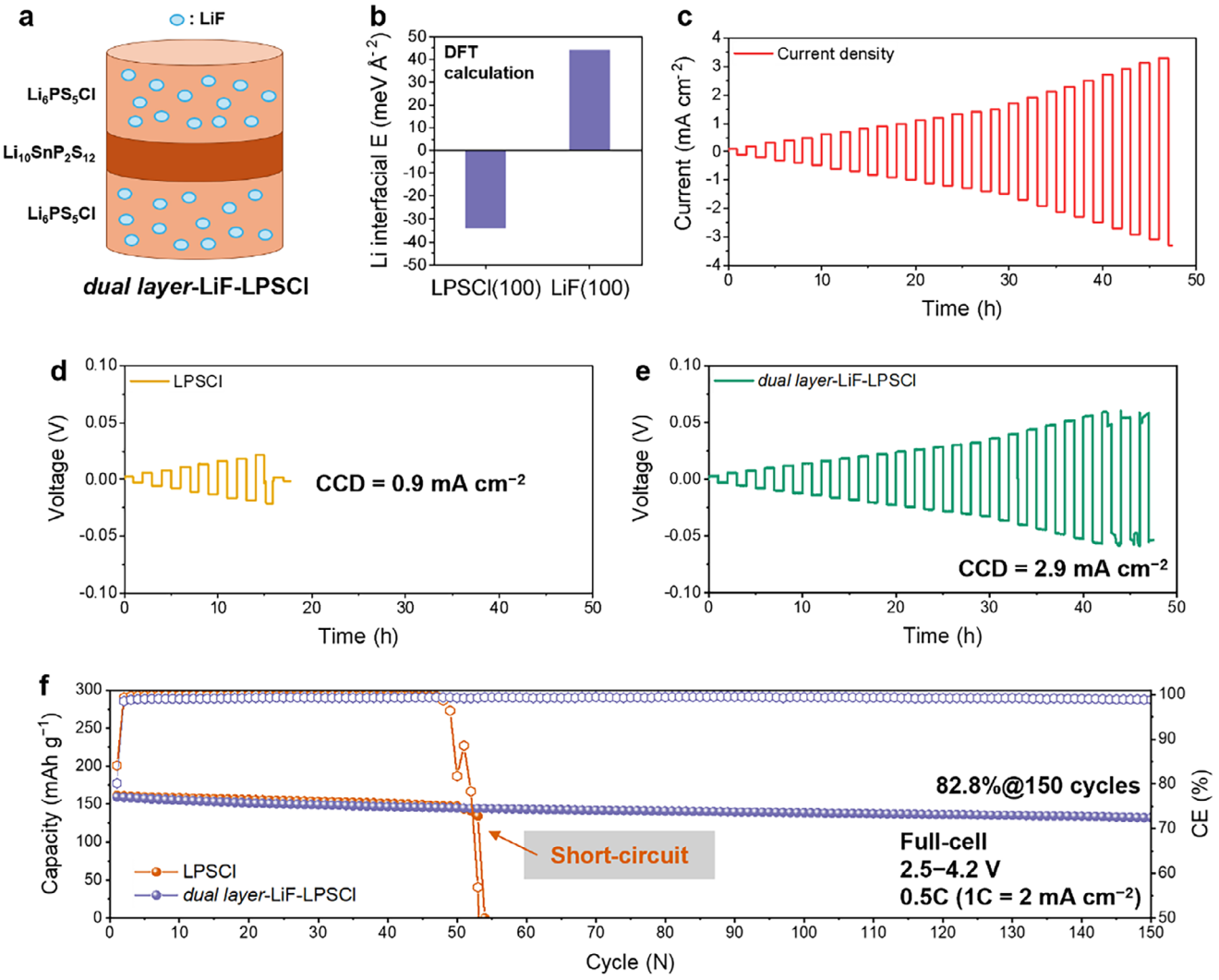

Figure 5. Solid electrolyte layer engineering with screw effect and Li interfacial energy control. a) Schematic illustration of dual-layered and LiF-enforced LPSCl (dual layer-LiF-LPSCl). b) DFT-calculated interfacial energies of the LPSCl(100) and LiF(100) facets against Li(100). c) Current density for CCD evaluations. Voltage profiles of the CCD evaluations of Li symmetric cells with d) bare LPSCl and e) dual layer-LiF-LPSCl solid electrolytes. f) Full-cell performances of the anode-less systems with a 100 nm-thick Mg thin-film protection layer using either bare LPSCl or dual layer-LiF-LPSCl as the solid electrolyte.

In full-cell configurations in which Mg thin-film anodes are paired with NCM811 cathodes, the cycle life of the cell with the dual layer-LiF-LPSCl solid electrolyte was extended markedly compared to that of its pristine solid electrolyte counterpart, which short-circuited after 50 cycles (Figure 5f). The dual layer-LiF-LPSCl cell maintained stable performance for 150 cycles at room temperature with 82.8% capacity retention (Figure 5f; Figure S25, Supporting Information), confirming the validity of our approach. Even under high cathode loading conditions (20 mg_{NCM} cm^{-2}), the system retained 83.6% of its capacity over 100 cycles (Figure S26, Supporting Information). This represents superior cycling performance among reported anode-less systems, particularly at room temperature (Table S1, Supporting Information). These results reveal that two critical tasks are necessary for advancing anode-less battery technology: 1) strategic composition screening for optimized anode-less seed layers and 2) innovative solid electrolyte engineering to mitigate short circuits.

3. Conclusion

This study involved a systematic investigation of anode-less battery systems in which lithiophilic metal thin-films were used as a protective interfacial layer between the anode-less electrode and the electrolyte. The performance of liquid and solid electrolyte configurations was compared. Six different representative lithiophilic metals were respectively deposited as 100 nm-thick thin-films on the anode current collector, in an effort to preserve the energy density while inducing uniform reversible Li (de)plating in the anode-less architectures. In the liquid electrolyte systems, all the metal candidates experienced severe capacity fading and exhibited poor reversibility, regardless of the chosen metal seed.

This behavior originates from the unconstrained 3D reaction interface between the deposited Li and the liquid medium, which accelerates parasitic side reactions and irreversible Li consumption. Contrary to this, the cyclability of solid-state systems was determined to critically depend on the characteristics of the protective layer, and Mg proved to be the optimal choice. Nevertheless, the solid-state systems remained susceptible to internal short-circuiting during extended cycling. To address this issue, we employed a solid electrolyte with a bilayer architecture, which gives rise to a screw effect, complemented by the incorporation of LiF as an additive to the solid electrolyte matrix to optimize the interfacial energy with Li metal. This synergistic strategy enabled the stable room-temperature operation of anode-less ASSBs. By elucidating the electrochemical and structural behaviors of lithiophilic metal thin-film layers in different physical states of electrolyte, this work identified solid electrolytes as the more suitable choice for enhancing the reversibility of anode-less systems. Importantly, within the domain of solid-state electrolytes, we demonstrated that short circuits can be effectively mitigated through tailored modifications of both the chemical and mechanical properties of the electrolyte, thereby providing a strategic framework for advancing anode-less battery technologies.

4. Experimental Section

Preparation of Electrode: Metal-coated copper (Cu) foil was prepared via a physical vapor deposition sputtering method. Cu foil (20 µm thickness) served as the substrate, with sputtering conducted under controlled conditions: DC power of 300 W, high-purity argon (Ar) as sputtering gas, 2 mTorr pressure, and a target-substrate distance of 150 mm. Six different metals—Ag, Al, In, Mg, Sn, and Zn—were utilized as targets, each of which was deposited to a thickness of 100 nm.

For full-cell evaluations with liquid electrolytes, cathodes were fabricated by blade coating a slurry composed of NCM811, Super P, and PVDF in a weight ratio of 95:3:2, with *N*-methyl pyrrolidone as the solvent. The components were uniformly dispersed using a Thinky mixer (Thinky Corporation, AR-100) before casting onto aluminum (Al) foil. The slurry was doctor-bladed to achieve an areal capacity of 2.0 mAh cm^{-2}, followed by drying in an oven at 80 °C for 12 h. The dried electrode underwent calendering via a roll-pressing process.

Composite cathodes for the solid-electrolyte-based full-cells were prepared by dispersing $LiNbO_3$-coated NCM811 (Wellcos Corp.), LPSCl (NEI Corp.), vapor-grown carbon fiber, and butadiene rubber binder in butyl butyrate at a weight ratio of 70:26:1.5:2.5. The resulting slurry was cast onto Al foil and dried at 100 °C for 12 h. For both the liquid- and solid-based systems, the mass loading of the cathode active material was maintained at 10 mg_{NCM} cm^{-2}. For the high-loading cathode full-cell evaluation, the active material mass loading was 20 mg_{NCM} cm^{-2}.

Cell Fabrication: The liquid-electrolyte-based experiments were conducted in CR2032 coin cells assembled in an argon-filled glovebox. PP2400 (Celgard) served as the separator, and 60 µL of electrolyte—composed of 3 M LiFSI in FSA solvent—was incorporated into each cell. The liquid half-cell contained a 300 µm-thick Li metal foil with a diameter of 12 mm.

The all-solid-state half-cells were assembled by first cold-pressing 100 mg of LPSCl into an SE layer (10 mm diameter) at 120 MPa. An anode-less electrode, consisting of a 100 nm metallic film deposited on Cu foil, was positioned beneath the SE layer, and the stack was compressed at 390 MPa. A Li foil counter electrode (300 µm-thick, 9.8 mm diameter) was then placed atop the SE layer. The assembled cell was transferred to a custom housing case equipped with a calibrated spring (Shinheung Indus.), which served to maintain a controlled stack pressure of 20 or 5 MPa during testing through its defined spring constant and adjustable depth.

For full-cell fabrication, the LPSCl SE layer was prepared identically to the half-cell procedure. The dual layer-LiF-LPSCl was fabricated using 20 mg of LSPS (NEI Corp.) powder as a base. Subsequently, 80 mg of LiF–LPSCl composite powder—prepared by homogeneously dry-mixing LPSCl and LiF (Nanorh) in a 95:5 wt% ratio (2000 rpm, 20 min)—was symmetrically distributed (40 mg per side) onto both surfaces of the LSPS. This structure underwent pressing (120 MPa) to ensure interfacial cohesion and mechanical integrity. The prefabricated composite cathode and anode-less electrode were symmetrically arranged on opposing sides of the SE pellet, followed by compression at 390 MPa. The cell was housed in a pressure-regulated case, with a 20 MPa stack pressure applied using the aforementioned spring mechanism. All assembly steps were conducted in an argon-filled glovebox to prevent moisture and oxygen contamination.

Characterization Methods: Top- and cross-sectional images of the electrodes were captured using field emission scanning electron microscopy (JSM-7800F Prime, JEOL), installed at the National Center for Inter-university Research Facilities. All electrochemical characterizations were performed at 25 °C. Half-cell tests employed a voltage cutoff of 0.1 V (vs Li/Li^+) during stripping, using a battery cycler (WBCS 3000, WonATech). Full-cells were cycled in a voltage window of 2.5–4.2 V (vs Li/Li^+), with charging in constant current–constant voltage (CC–CV) mode and discharging in CC mode, utilizing the same instrument. The CV cutoff current was set to 0.05 C. EIS measurements were conducted using a half-cell configuration with a potentiostat (VSP, Bio-Logic).

Computational Details: DFT calculations were conducted employing the Vienna Ab initio Simulation Package,[28] utilizing the Perdew–Burke–Ernzerhof[29] exchange-correlation functional and the projector-augmented wave method.[30] A plane-wave energy cutoff of 520 eV and a Monkhorst–Pack *k*-point mesh with a grid spacing of 0.03 $Å^{-1}$ were adopted to ensure convergence. Electronic and ionic relaxations were considered complete at energy and force thresholds of 10^{-7} eV and 0.02 eV $Å^{-1}$, respectively. Interface energies were evaluated using a linear extrapolation scheme, as implemented in a prior methodology.[31]

Supporting Information

Supporting Information is available from the Wiley Online Library or from the author.

Acknowledgements

J.O., J.K., and S.B. contributed equally to this work. J.W.C. acknowledges the National Research Foundation of Korea (NRF) (RS-2024-00335274, RS-2023-00261543) and the Swiss National Science Foundation (SNF) (Sinergia CRSII5_202296). J.W.C. also acknowledges support from the Institute of Engineering Research (IOER), the Research Institute of Advanced Materials (RIAM), and the Institute for Battery Research Innovation (IBRI) at Seoul National University. H.K. acknowledges support from the Korea Basic Science Institute (C512310).

Conflict of Interest

The authors declare no conflict of interest.

Data Availability Statement

The data that support the findings of this study are available from the corresponding author upon reasonable request.

Keywords

all-solid-state batteries, anode-less, liquid electrolyte, lithiophilic seed, solid electrolyte

Received: May 18, 2025
Revised: July 13, 2025
Published online: July 30, 2025

[1] a) R. Van Noorden, *Nature* **2014**, *507*, 26; b) X. He, D. Bresser, S. Passerini, F. Baakes, U. Krewer, J. Lopez, C. T. Mallia, Y. Shao-Horn, I. Cekic-Laskovic, S. Wiemers-Meyer, F. A. Soto, V. Ponce, J. M. Seminario, P. B. Balbuena, H. Jia, W. Xu, Y. Xu, C. Wang, B. Horstmann, R. Amine, C.-C. Su, J. Shi, K. Amine, M. Winter, A. Latz, R. Kostecki, *Nat. Rev. Mater.* **2021**, *6*, 1036; c) I. Kim, H. Kim, S. An, J. Oh, M. Kim, J. W. Choi, *Energy Environ. Sci.* **2025**, *18*, 3784.

[2] a) Y. Wen, K. He, Y. Zhu, F. Han, Y. Xu, I. Matsuda, Y. Ishii, J. Cumings, C. Wang, *Nat. Commun.* **2014**, *5*, 4033; b) M. Ko, S. Chae, J. Ma, N. Kim, H.-W. Lee, Y. Cui, J. Cho, *Nat. Energy* **2016**, *1*, 16113.

[3] a) T. Lee, M. J. Seong, H. C. Ahn, M. Baek, K. Park, J. Oh, T. Choi, J. W. Choi, *Proc. Natl. Acad. Sci. USA* **2025**, *122*, 2417053121; b) C. K. Chan, H. Peng, G. Liu, K. McIlwrath, X. F. Zhang, R. A. Huggins, Y. Cui, *Nat. Nanotechnol.* **2008**, *3*, 31.

[4] a) N. Lee, J. Oh, J. W. Choi, *Mater. Futures* **2023**, *2*, 013502; b) J. Qian, B. D. Adams, J. Zheng, W. Xu, W. A. Henderson, J. Wang, M. E. Bowden, S. Xu, J. Hu, J.-G. Zhang, *Adv. Funct. Mater.* **2016**, *26*, 7094.

[5] a) M. Tang, S. Dong, J. Wang, L. Cheng, Q. Zhu, Y. Li, X. Yang, L. Guo, H. Wang, *Nat. Commun.* **2023**, *14*, 6006; b) G. Deysher, J. A. S. Oh, Y.-T. Chen, B. Sayahpour, S.-Y. Ham, D. Cheng, P. Ridley, A. Cronk, S. W.-H. Lin, K. Qian, L. H. B. Nguyen, J. Jang, Y. S. Meng, *Nat. Energy* **2024**, *9*, 1161.

[6] a) R. Weber, M. Genovese, A. J. Louli, S. Hames, C. Martin, I. G. Hill, J. R. Dahn, *Nat. Energy* **2019**, *4*, 683; b) S. Liu, X. Yu, Y. Yan, T. Zeng, X. Wang, G. Tian, C. Wang, S. Wang, Y. Zeng, C. Shu, *Energy Storage Mater.* **2023**, *62*, 102959.

[7] L. Braks, J. Zhang, A. Forster, P. Fritz, J. Oh, M. El Kazzi, J. W. Choi, A. Coskun, *Angew. Chem., Int. Ed.* **2024**, *63*, 202408238.

[8] a) J. Oh, S. H. Choi, H. Kim, J. Y. Kim, G.-J. Lee, K. Y. Bae, T. Lee, N. Lee, Y. Sohn, W. J. Chung, J. W. Choi, *Energy Environ. Sci.* **2024**, *17*, 7932; b) S. Nanda, A. Gupta, A. Manthiram, *Adv. Energy Mater.* **2021**, *11*, 2000804; c) Y. Qiao, H. Yang, Z. Chang, H. Deng, X. Li, H. Zhou, *Nat. Energy* **2021**, *6*, 653; d) Y. Xu, H. Zheng, H. Yang, Y. Yu, J. Luo, T. Li, W. Li, Y.-N. Zhang, Y. Kang, *Nano Lett.* **2021**, *21*, 8664.

[9] Y. Zhou, P. Wang, K. Wang, X. Fang, W. Li, J. Nai, Y. Liu, Y. Wang, S. Zou, H. Yuan, X. Tao, J. Luo, *Adv. Funct. Mater.* **2025**, *35*, 2424022.

[10] Y.-G. Lee, S. Fujiki, C. Jung, N. Suzuki, N. Yashiro, R. Omoda, D.-S. Ko, T. Shiratsuchi, T. Sugimoto, S. Ryu, J. H. Ku, T. Watanabe, Y. Park, Y. Aihara, D. Im, I. T. Han, *Nat. Energy* **2020**, *5*, 299.

[11] J. Oh, S. H. Choi, B. Chang, J. Lee, T. Lee, N. Lee, H. Kim, Y. Kim, G. Im, S. Lee, J. W. Choi, *ACS Energy Lett.* **2022**, *7*, 1374.

[12] a) J. Lee, S. H. Choi, G. Im, K.-J. Lee, T. Lee, J. Oh, N. Lee, H. Kim, Y. Kim, S. Lee, J. W. Choi, *Adv. Mater.* **2022**, *34*, 2203580; b) Z. T. Wondimkun, W. A. Tegegne, J. Shi-Kai, C.-J. Huang, N. A. Sahalie, M. A. Weret, J.-Y. Hsu, P.-L. Hsieh, Y.-S. Huang, S.-H. Wu, W.-N. Su, B. J. Hwang, *Energy Storage Mater.* **2021**, *35*, 334; c) S. Cho, D. Y. Kim, J.-I. Lee, J. Kang, H. Lee, G. Kim, D.-H. Seo, S. Park, *Adv. Funct. Mater.* **2022**, *32*, 2208629; d) X. Li, Y. Su, Y. Qin, F. Huang, S. Mei, Y. He, C. Peng, L. Ding, Y. Zhang, Y. Peng, Z. Deng, *Adv. Mater.* **2023**, *35*, 2303489.

[13] a) J. Oh, S. H. Choi, J. Y. Kim, J. Lee, T. Lee, N. Lee, T. Lee, Y. Sohn, W. J. Chung, K. Y. Bae, S. Son, J. W. Choi, *Adv. Energy Mater.* **2023**, *13*, 2301508; b) S.-J. Jeon, C. Hwang, H.-S. Kim, J. Park, J.-Y. Hwang, Y. Jung, R. Choi, M.-S. Song, Y. J. Lee, J.-S. Yu, Y.-C. Jung, *Adv. Energy Mater.* **2024**, *14*, 2402887.

[14] S. S. Zhang, X. Fan, C. Wang, *Electrochim. Acta* **2017**, *258*, 1201.

[15] a) L. Ye, X. Li, *Nature* **2021**, *593*, 218; b) L. Ye, Y. Lu, Y. Wang, J. Li, X. Li, *Nat. Mater.* **2024**, *23*, 244.

[16] a) Y. Sohn, J. Oh, J. Lee, H. Kim, I. Hwang, G. Noh, T. Lee, J. Y. Kim, K. Y. Bae, T. Lee, N. Lee, W. J. Chung, J. W. Choi, *Adv. Mater.* **2024**, *36*, 2407443; b) J. Pu, J. Li, K. Zhang, T. Zhang, C. Li, H. Ma, J. Zhu, P. V. Braun, J. Lu, H. Zhang, *Nat. Commun.* **2019**, *10*, 1896; c) Y. Wang, J. Tan, Z. Li, L. Ma, Z. Liu, M. Ye, J. Shen, *Energy Storage Mater.* **2022**, *53*, 156.

[17] S.-K. Otto, T. Fuchs, Y. Moryson, C. Lerch, B. Mogwitz, J. Sann, J. Janek, A. Henss, *ACS Appl. Energy Mater.* **2021**, *4*, 12798.

[18] M. C. Schulze, N. R. Neale, *ACS Energy Lett.* **2021**, *6*, 1082.

[19] A. J. Louli, A. Eldesoky, R. Weber, M. Genovese, M. Coon, J. deGooyer, Z. Deng, R. T. White, J. Lee, T. Rodgers, R. Petibon, S. Hy, S. J. H. Cheng, J. R. Dahn, *Nat. Energy* **2020**, *5*, 693.

[20] a) J. Oh, W. J. Chung, S. H. Jung, Y. Kim, Y. Lee, Y. J. Nam, S. Lee, C. H. Kim, J. W. Choi, *Energy Storage Mater.* **2024**, *71*, 103606; b) M. Baek, J. Kim, K. Jeong, S. Yang, H. Kim, J. Lee, M. Kim, K. J. Kim, J. W. Choi, *Nat. Commun.* **2023**, *14*, 1296.

[21] a) J. Gu, X. Chen, Z. He, Z. Liang, Y. Lin, J. Shi, Y. Yang, *Adv. Energy Mater.* **2023**, *13*, 2302643; b) C. Yuan, W. Lu, J. Xu, *Adv. Energy Mater.* **2021**, *11*, 2101807.

[22] a) J. Oh, D. Kwon, S. H. Choi, N. Lee, Y. Sohn, T. Lee, T. Lee, J. Y. Kim, K. Y. Bae, J. W. Choi, *Adv. Energy Mater.* **2025**, *15*, 2404817; b) Y. Ye, H. Xie, Y. Yang, Y. Xie, Y. Lu, J. Wang, X. Kong, S. Jin, H. Ji, *J. Am. Chem. Soc.* **2023**, *145*, 24775.

[23] D. Jun, S. H. Park, J. E. Jung, S. G. Lee, K. S. Kim, J. Y. Kim, K. Y. Bae, S. Son, Y. J. Lee, *Adv. Funct. Mater.* **2024**, *34*, 2310259.

[24] T. Krauskopf, B. Mogwitz, C. Rosenbach, W. G. Zeier, J. Janek, *Adv. Energy Mater.* **2019**, *9*, 1902568.

[25] T. H. Wan, M. Saccoccio, C. Chen, F. Ciucci, *Electrochim. Acta* **2015**, *184*, 483.

[26] N. Lee, J. Lee, T. Lee, J. Oh, I. Hwang, G. Seo, H. Kim, J. W. Choi, *ACS Appl. Mater. Interfaces* **2023**, *15*, 34931.

[27] J. Oh, J. Frank, R. Leising, H. Kim, J. Kim, M. Kim, J. W. Choi, *Energy Environ. Sci.* **2025**, https://doi.org/10.1039/D5EE01490E.

[28] G. Kresse, J. Furthmüller, *Comput. Mater. Sci.* **1996**, *6*, 15.

[29] J. P. Perdew, K. Burke, M. Ernzerhof, *Phys. Rev. Lett.* **1996**, *77*, 3865.

[30] P. E. Blöchl, *Phys. Rev. B* **1994**, *50*, 17953.

[31] N. D. Lepley, N. A. W. Holzwarth, *Phys. Rev. B* **2015**, *92*, 214201.